



Demystifying role of local distortion in emission colors tuning of lead-free zero-dimensional metal halide nanocrystals



Tuhin Samanta ^{a,1}, Noolu Srinivasa Manikanta Viswanath ^{a,1}, Hyeon Woo Kim ^{b,c}, Sung Woo Jang ^a, Joo Hyeong Han ^a, Sung Beom Cho ^c, Won Bin Im ^{a,*}

^a Division of Materials Science and Engineering, Hanyang University, 222 Wangsimni-ro, Seongdong-gu, Seoul 04763, Republic of Korea

^b Nano Convergence Materials Center, Emerging Materials R&D Division, Korea Institute of Ceramic Engineering and Technology (KICET), 101 Soho-ro, Jinju-si, 52851, Republic of Korea

^c Department of Materials Science and Engineering and Department of Energy Systems Research, Ajou University, Suwon-si 16499, Republic of Korea

ARTICLE INFO

Keywords:

Self-trapped emission
Local distortion
Zero-dimensional metal halides
and color tunability

ABSTRACT

Photoluminescence (PL) systems that display emission color tuning have recently gained importance because of their significant role in lighting technologies. However, lead-free metal halides (MHs) for tuning emission wavelengths remain elusive owing to their large bandgaps. Herein, the synthesis of a series of highly luminescent lanthanide (Ln)-based zero-dimensional $\text{Cs}_3\text{LnCl}_6:\text{Sb}^{3+}$ ($\text{CLnC}:\text{Sb}^{3+}$) nanocrystals (NCs), where $\text{Ln} = \text{Lu}^{3+}, \text{Y}^{3+}, \text{Gd}^{3+}$, or La^{3+} , exhibiting tunable emission colors are demonstrated. Structural and density functional theory calculations revealed a direct relationship between the size and local distortion of the LnCl_6 polyhedra and, hence, the emitting center, the SbCl_6 octahedra. In particular, when the size of LnCl_6 increased, the degree of local distortion increased from Lu to La, which enabled tuning of the emission wavelengths. Furthermore, a white-light-emitting device was constructed using $\text{CLaC}:\text{Sb}^{3+}$ NCs, which delivered a high color rendering index of 93. The results of this study will pave the way for achieving tunable emission energies in other low-dimensional MHs for next-generation lighting applications.

1. Introduction

Self-trapped exciton (STE) luminescent materials have recently gained special attention owing to their remarkable optical properties such as a large Stokes shift (which ensures negligible self-absorption) and high photoluminescence quantum yields (PLQYs). Considering their high PLQY and large Stokes shift, these STE emitters are promising for solid-state lighting, scintillation, and luminescent solar concentrator applications [1,2,3–9].

Three-dimensional Pb halide perovskites (LHPs) possess a potential barrier for self-trapping, which can promote the recombination of photo excited charge carriers as free exciton (FE) luminescence [10]. However, two-dimensional (2D) LHPs exhibit broad emissions originating from the combination of FE and STE emission, such as N-MEDA($\text{PbBr}_{4-x}\text{Cl}_x$) and $\text{EA}_4\text{Pb}_3\text{Cl}_{10-x}\text{Br}_x$ [11–13]. This is because of the large organic group at the A-site and mixed halides, and the Pb-halide octahedra and inorganic framework experience distortion to some extent, which can be evaluated using the interoctahedral tilt (Θ_{tilt}) [14,15]. Therefore, the

STE property of LHPs depends solely on the structural distortion. However, in 2D LHPs, the photo generated carriers are delocalized in the interconnected octahedra, whereas in zero-dimensional (0D) metal halides (MHs), charge carriers are confined in isolated octahedra and thus experience a strong confinement effect. Moreover, 0D MHs have no interconnected framework (that is, MH octahedra are isolated from each other), and hence, there is no conception of Θ_{tilt} . Consequently, an energy barrier between the FE and STE states does not exist in 0D STE emitters. Therefore, these aspects indicate that 0D MHs have significantly higher PLQY values than 2D LHPs. Furthermore, 0D MHs can be synthesized as colloidal solutions, providing excellent colloidal stability when compared to other high-dimensional metal halides and also demonstrating good stability under ambient conditions, ensuring that their unique properties are maintained over time. Hence, highly efficient 0D MHs must be developed for solid-state lighting applications.

Among the various dopants explored for use in 0D MHs for bright STE emission, Sb^{3+} ions are particularly promising. Sb^{3+} -doped 0D MHs, namely $\text{Rb}_3\text{InCl}_6:\text{Sb}^{3+}$ [16], $\text{Cs}_3\text{ScCl}_6:\text{Sb}^{3+}$ [17], $\text{Cs}_2\text{SnCl}_6:\text{Sb}^{3+}$ [18],

* Corresponding author.

E-mail address: imwonbin@hanyang.ac.kr (W.B. Im).

¹ Authors are equally contributed to this work.

$\text{Rb}_4\text{CdCl}_6:\text{Sb}^{3+}$ [19], and $\text{Cs}_2\text{ZnCl}_4:\text{Sb}^{3+}$ [20], exhibit bright green, yellow, blue, and red emissions, respectively. Although these materials belong to the 0D MH family and involve emissions from the Sb octahedra, they exhibit different emission colors. Furthermore, it has been illustrated that by reducing dimensionality, the emission colors can be systematically tuned across the spectral range from blue to red. This tunability is attributed to the heightened degree of asymmetry achieved through the incorporation of Sb^{3+} -ions into the lattice site during the alteration of dimensionality [21,22]. To date, no studies have investigated the impact of local distortion on the color tuning emission properties of lead-free metal halide nanocrystals. This specific research area remains largely unexplored, especially within the context of zero-dimensional materials. Therefore, it is important to understand the fundamental aspects of emission tuning to propose a plausible mechanism.

In this work, a series of lanthanide (Ln)-based 0D MHs, namely $\text{Cs}_3\text{LuCl}_6:\text{Sb}^{3+}$ ($\text{CLuC}:\text{Sb}^{3+}$), $\text{Cs}_3\text{YCl}_6:\text{Sb}^{3+}$ ($\text{CYC}:\text{Sb}^{3+}$), $\text{Cs}_3\text{GdCl}_6:\text{Sb}^{3+}$ ($\text{CGC}:\text{Sb}^{3+}$), and $\text{Cs}_3\text{LaCl}_6:\text{Sb}^{3+}$ ($\text{CLaC}:\text{Sb}^{3+}$) nanocrystals (NCs), were synthesized in this study using the hot-injection method. These MHs exhibited broad emission with tunable peak wavelengths of 520–570 nm depending on the Ln ion. Structural and density functional theory (DFT) calculations were performed to understand the origin of the tunable emission colors of these compounds. Based on the obtained results, we proposed a plausible mechanism for tuning the emission color of this 0D MH family. The synthesized NCs were tested in white light-emitting diode (WLED) applications to determine their practical feasibility.

2. Experimental section

2.1. Chemicals

Cesium carbonate (Cs_2CO_3 , 99 %), yttrium (III) acetate hydrate (99.9 %), gadolinium (III) acetate hydrate (99.9 %), lanthanum (III) acetate hydrate (99.9 %), benzoyl chloride, 1-octadecene (ODE, 99 %), oleylamine (OM, 98 %), oleic acid (OA, 90 %), hexane (anhydrous, 95 %), ethyl acetate (anhydrous, 99.8 %) were purchased from Sigma-Aldrich. Lutetium (III) acetate hydrate (99.9 %) was purchased from Alfa Aesar. All chemicals were used without any further purification.

2.2. Synthesis method

In a typical synthesis process, 0.45×3 mmol Cs_2CO_3 , 0.45×0.98 mmol lanthanum acetate, 0.02 mmol antimony acetate, 6 mL ODE, 3 mL OA, and 1.5 mL OLA were added in a 20-mL vial. The reaction mixture was degassed under a vacuum for 60 min. Subsequently, the vial was filled with N_2 gas. The vial was heated on a hotplate up to 120 °C for 60 min to completely dissolve the Cs_2CO_3 , scandium acetate, and antimony acetate. After that, the reaction mixture was heated from 120 to 220 °C. At that temperature, a solution of 400 μL benzoyl chloride in 0.7 mL of degassed ODE was briskly injected into the vial. Immediately after the injection, the vial was cooled down by an ice-water bath. Then, 5 mL of hexane was added to the solution. The reaction mixture was centrifuged at 8000 rpm for 5 min, and the supernatant was decanted. The precipitated nanoparticles were redispersed in 5 mL of hexane and centrifuged at 4000 rpm for 5 min. The supernatant was collected and precipitated by adding 5 mL ethyl acetate and centrifuged at 5000 rpm for 5 min. The precipitated nanoparticles were redispersed in 5 mL hexane and centrifuged at 5000 rpm for 5 min. The supernatant $\text{Cs}_3\text{La}_{0.98}\text{Sb}_{0.02}\text{Cl}_6$ NCs was stored for further characterization. The $\text{Cs}_3\text{Gd}_{0.98}\text{Sb}_{0.02}\text{Cl}_6$, $\text{Cs}_3\text{Y}_{0.98}\text{Sb}_{0.02}\text{Cl}_6$, and $\text{Cs}_3\text{Lu}_{0.98}\text{Sb}_{0.02}\text{Cl}_6$ NCs were also synthesized using the similar protocol of $\text{Cs}_3\text{La}_{0.98}\text{Sb}_{0.02}\text{Cl}_6$ NCs.

2.3. Structural and morphology characterizations

The structures of the as-synthesized samples were characterized by XRD (Miniflex 600) using a diffracted beam monochromator set for Cu-

$\text{K}\alpha$ radiation ($\lambda = 1.54056 \text{ \AA}$). The 2θ scan range was 10°–100° with a step size of 0.01°. Structural information was derived from Rietveld refinement using the GSAS software suite. A three-dimensional visualization system for electronic and structural analysis (VESTA) was used to draw the crystal structures. The phase purity of the as-synthesized samples was estimated via Rietveld refinement of the XRD results with the consideration of full refinement of the crystallographic and instrumental parameters in the GSAS program suite. HR-TEM images were obtained using a JEOL JEM-2100F microscope.

2.4. Optical characterizations

Steady-state PL spectra of the samples were recorded using a Hitachi F-7000 fluorescence spectrophotometer. The variation in PL intensity during heating was measured by connecting a Hitachi F-7000 fluorescence spectrometer to an integrated heater, temperature controller, and thermal sensor. A time-correlated single-photon counting system (TimeHarp-260, PicoQuant GmbH, Germany) was used to count the emitted photons. The PLQYs of the as-synthesized samples were measured using a HORIBA FluoroMax Plus spectrofluorometer. X-ray photoelectron spectra (XPS) of the samples were measured in Thermo-fisher scientific (Nexsa G2) instrument. Thermo-fisher scientific Nexsa is a fully integrated XPS instrument, with low power Al Kα X-ray source, 10–400 μm (adjustable in 5 μm steps), 3600 mm^2 (600 mm × 600 mm) sample area, 20 mm sample thickness. The absolute PLQY of the samples were measured using a HORIBA FluoroMax Plus spectrofluorometer paired with K-sphere petite internal, directly coupled with Integrating Sphere. The excitation source was standard 75 W xenon arc, attached to the front of QM sample compartment.

2.5. Computational calculations

Density functional theory (DFT) calculations were performed with the Vienna Ab initio Simulation Package (VASP) using the projector augmented-wave method with generalized gradient approximation (GGA) within the Perdew–Burke–Ernzerhof (PBE) framework. The plane-wave basis set was expanded to cutoff energy of 520 eV to minimize Pulay stress during the structural optimization. The structural optimization was truncated until the Hellmann–Feynman forces were under 0.01 eV/Å. Electronic energy convergence was set to 1×10^{-5} eV. The Brillouin zone was sampled using 100 k -points density per inverse Å³ of reciprocal cell. At the same level of theory, a systematic elongation of the axial Sb–Cl bonds was conducted, ranging from the ground state equilibrium value of 2.67 Å to a maximum value of 3.13 Å with steps of 0.025 Å.

2.6. Prototype WLED fabrication

Prototype WLED devices were fabricated using $\text{CLaC}:\text{Sb}^{3+}$ powder on an InGaN LED chip ($\lambda_{\text{max}} = 365 \text{ nm}$). The devices were then encapsulated in a $\text{CLaC}:\text{Sb}^{3+}$ /silicone resin mixture, with the mixture placed directly on the headers and then cured at 60 °C for 1 h. After packaging, the WLED device was measured in an integrating sphere under a direct-current forward-bias condition.

3. Results and discussion

$\text{Cs}_3\text{LnCl}_6:\text{Sb}^{3+}$ ($\text{CLnC}:\text{Sb}^{3+}$), where $\text{Ln} = \text{Lu}, \text{Y}, \text{Gd}$, or La , crystallizes into a monoclinic crystal structure with a non-centrosymmetric space group of $C2/c$. $\text{CLnC}:\text{Sb}^{3+}$ consists of an asymmetrical framework composed of three Cs sites, two Ln sites, and five Cl sites for CLuC, and seven Cl sites for CYC, CGC, and CLaC. Each Ln atom, where $\text{Ln} = \text{Lu}, \text{Y}, \text{Gd}$, or La , bonds with six Cl atoms to form an octahedron, as shown in Fig. 1a [23]. Moreover, the $[\text{LnCl}_6]^{3-}$ octahedra are isolated from one another by Cs^+ ions, forming a 0D structure. To determine the phase purity of the as-synthesized samples, a Rietveld refinement analysis was

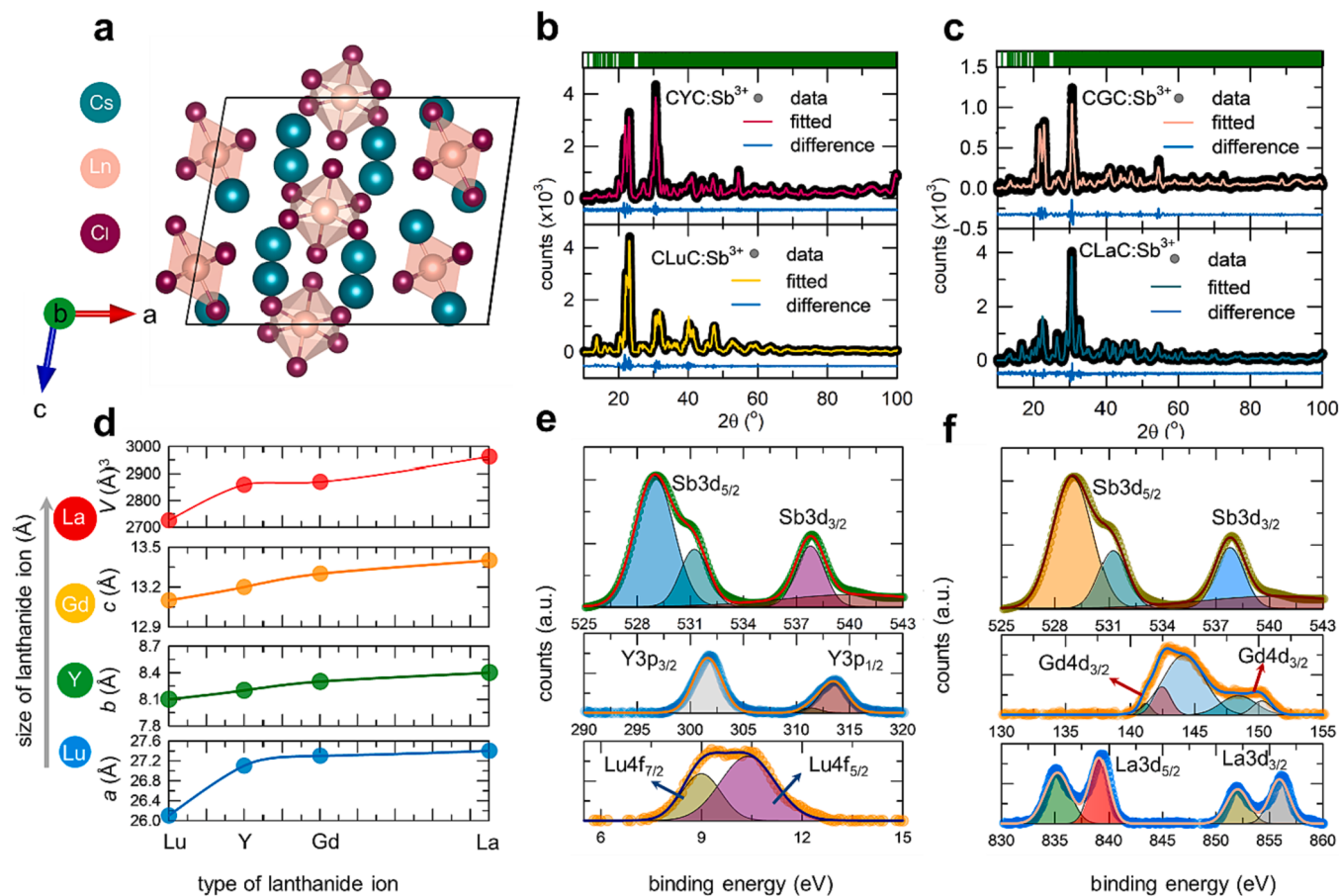


Fig. 1. Structural properties of CLnC: Sb³⁺ NCs. (a) crystal structure of CLnC: Sb³⁺ NCs, where dark cyan, peach, and dark pink represents the Cs, Ln, and Cl atoms, respectively. (b) and (c) Rietveld refinement plots of CLnC: Sb³⁺ NCs, after full pattern fitting: Observed (black dots), calculated (dark pink (CYC: Sb³⁺), yellow (CLuC: Sb³⁺), orange (CGC: Sb³⁺), and dark cyan (CLaC: Sb³⁺) lines), and the difference (blue lines), respectively. (d) Shows plot of lattice parameter and cell volume against the size of lanthanide ion in CLnC: Sb³⁺ NCs derived from Reitveld refinement analysis. (e) and (f) represent the Lu 4f, Y 3p, Gd 4d, La 3d, and Sb 3d regions of XPS spectra of CLnC: Sb³⁺ NCs. (For interpretation of the references to color in this figure legend, the reader is referred to the web version of this article.)

performed using GSAS software [24]. The refinement results suggested that the targeted compositions were formed without secondary phases (Fig. 1b and c). The detailed information about the refined structural and residual parameters are listed in Tables S1–S5. Furthermore, we measured the XRD patterns of CLnC, where Ln = Lu, Y, Gd, and La also indexed their corresponding lattice plans are shown in Fig. S1. In addition, the lattice parameters and cell volumes of CLnC:Sb³⁺ were also calculated. As shown in Fig. 1d, the lattice parameters and cell volume increased with an increasing Ln ion size due to differences in their ionic radii.

To determine the site selectivity of Sb³⁺ ions, the formation energies of the CLnC:Sb³⁺ NCs when Sb³⁺ ions were substituted at two distinct Ln sites were calculated using DFT calculations. The results indicated that when Sb³⁺ ions enter the Ln1 site, the formation energy is higher than that at the Ln2 site (Figure S2). Therefore, the Ln1 site is energetically favorable for the substitution of Sb³⁺ ions.

The chemical valences of the as-synthesized NCs were determined using X-ray photoelectron spectroscopy (XPS). Fig. 1e and f display the XPS spectra for Lu 4f, Y 3p, Gd 4d, La 3d, and Sb 3d, each with specific excitation energies as follows: 9.1 eV and 11.2 eV for Lu, 303 eV and 314 eV for Y, 139 eV, 142 eV, 145 eV, 147 eV, and 150 eV for Gd, 835 eV, 839 eV, 853 eV, and 857 eV for La, and 528 eV, 532 eV, and 538 eV for Sb. These results revealing that Lu, Y, Gd, La, and Sb ions coexisted in the + 3-oxidation state in the CLnC lattice (Fig. 1e and f), further confirming that Sb³⁺ ions were successfully doped into the monoclinic crystal structure of the host. The elemental maps in Figure S3, demonstrate Cs, Lu, Y, Gd, and La, Sb atoms are uniformly distributed

throughout the nanocrystals. The elemental composition of Cs: Lu/Y/Gd/La: Cl is found to be 3:1:6 (see Table S6,) which further confirms the targeted compositions have been formed.

To investigate the morphology and determine the particle size of the as-synthesized samples, high-resolution transmission electron microscopy (HR-TEM) images of the CLnC:Sb³⁺ NCs were acquired. First, HR-TEM images of the CLuC:Sb³⁺ NCs were collected, which showed that they were irregular in shape and agglomerated (Fig. 2a). The average NC particle size was approximately 18 nm. The NC lattice plane spacing of 0.27 nm corresponded to the (404) plane (Fig. 2b), which is consistent with the crystallographic data for CLuC. The bright spots arranged in concentric circles in Fig. 2c represent the selected-area electron diffraction (SAED) patterns of the CLuC lattice planes. The particle size of the CYC:Sb³⁺ NCs was measured using the HR-TEM image, which showed that they were spherical in shape (Fig. 2d) with a particle size of approximately 21 nm. The calculated lattice plane distance for the (11-2) plane was 0.524 nm (Fig. 2e), which is consistent with the crystallographic data for CYC. Furthermore, the SAED patterns (Fig. 2f) representing the lattice planes of CYC were also measured. The CGC: Sb³⁺ NCs exhibited a distorted hexagonal shape (Fig. 2g) with a particle size of approximately 23 nm. The calculated lattice plane was approximately 0.408 nm, corresponding to the (511) lattice plane (Fig. 2h), thus validating the crystallographic data of the CGC. As shown in Fig. 2i, the SAED patterns further confirmed the crystal lattice information of the CGC. The HR-TEM image of the CLaC:Sb³⁺ NCs shows that they had an irregular shape and an average particle size of approximately 65 nm (Fig. 2j). The calculated lattice plane distance for the (422) plane was

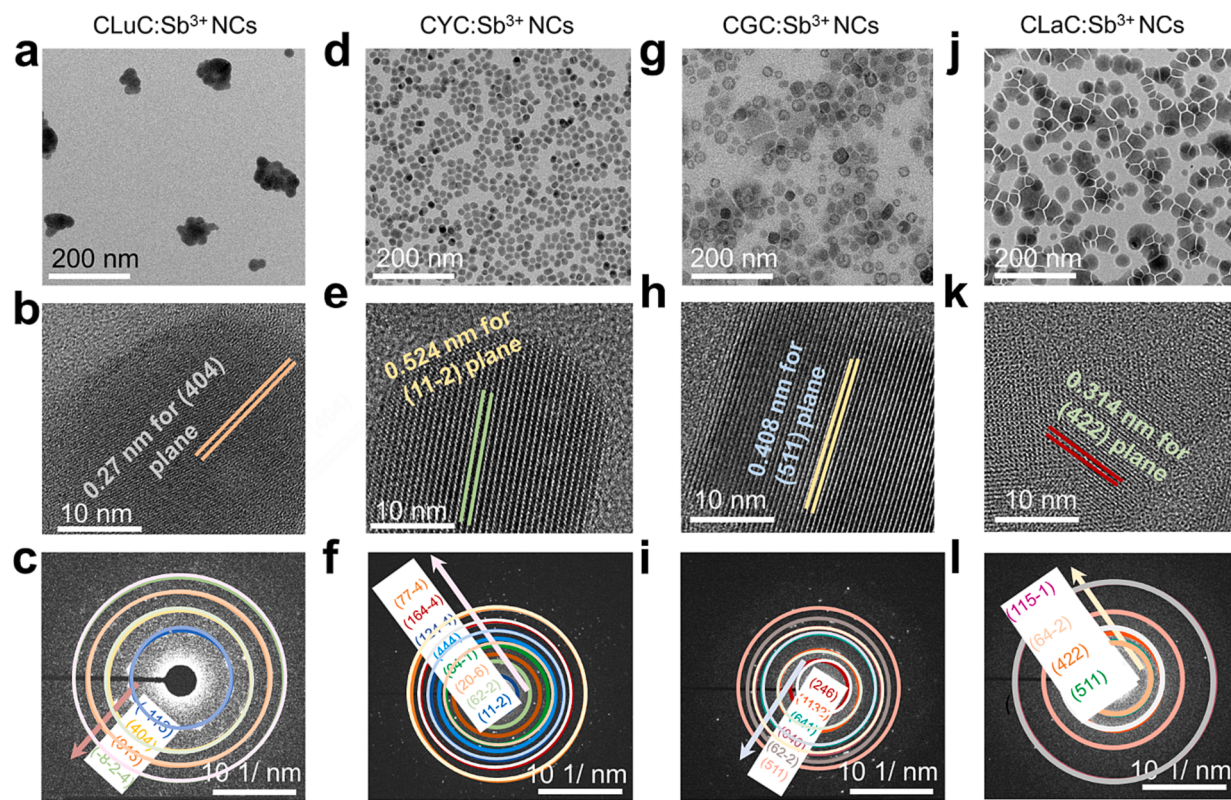


Fig. 2. The morphology of CLnC: Sb³⁺ NCs. (a), (b) and (c) shows HR-TEM image, lattice plane distance, and SAED patterns of CLuC:Sb³⁺ NCs.(d), (e), and (f) represents HR-TEM image, lattice plane distance, and SAED patterns of CYC:Sb³⁺ NCs. (g), (h), and (i) illustrates HR-TEM image, lattice plane distance, and SAED patterns of CGC:Sb³⁺ NCs. (j), (k), and (l) display the HR-TEM image, lattice plane distance, and SAED patterns of CLaC:Sb³⁺ NCs, wherein the arrow's orientation (Fig. 2c, f, i, and l) signifies the alignment of lattice planes about their concentric circles, respectively.

0.314 nm (Fig. 2k), which is in good agreement with the crystallographic data for CLaC. Fig. 2l clearly shows that the bright spots were arranged in concentric circles, representing the SAED patterns of the CLaC lattice planes. However, these results suggest the formation of phase-pure materials. Moreover, the luminescence properties of these NCs may not depend on their shape because the emission originates from the dopant Sb³⁺ ions.

To investigate the luminescence properties of the as-synthesized CLnC:Sb³⁺ NCs, the photoluminescence (PL) properties of the CLnC: Sb³⁺ NCs were recorded by excitation with a 320 nm light, which showed a broad emission band that is a typical STE-assisted emission upon doping of Sb³⁺ ions into the host lattice of CLnC [25]. However, when the Ln ion type was switched from Lu to La, the emission wavelength shifted from 525 to 570 nm (Fig. 3a). However, the shape of the excitation spectrum remained the same. Typically, the emission color in Sb³⁺-doped zero-dimensional metal halides is contingent upon the degree of asymmetry inherent in the Sb³⁺-doped lattice site. Illustratively, Rb₃InCl₆:Sb³⁺ exhibits green emission, while Cs₂InCl₅·H₂O:Sb³⁺ displays red emission. The diverse emission colors arise from variations in the degree of asymmetry within each Sb³⁺-doped lattice site. Additionally, the distinct crystal structures of these materials contribute to different excitation spectra. However, in similar crystal structure systems, the emission color is primarily governed by the degree of asymmetry present in the Sb³⁺-doped lattice site. Upon changing the Ln ion type from Lu to La, the PLQY progressively increased (Fig. 3b) and maximum PLQY obtained for CLaC:Sb³⁺ NCs, are compared with the reported PLQY values of Sb³⁺-based OD MH NCs (Table S7). Moreover, a PL decay analysis was performed on the as-synthesized CLnC:Sb³⁺ NCs. Fig. 3c and d shows that the average lifetime of the NCs increased from 2.8 to 5.4 μs when the Ln ion was changed from Lu to La. As it is important to note that there is a direct correlation is often observed

between a high PLQY and a long lifetime. When a material efficiently converts absorbed photons into emitted photons, it tends to have a longer lifetime because the radiative recombination process, responsible for luminescence, dominates over non-radiative processes.

The local structure plays an important role in tuning the emission wavelengths and improving the PLQY values of given luminescence materials [26]. Moreover, depending on the Ln ion size, the material will experience different local structural distortion [27]. For example, a smaller Ln ion, as compared with a larger Ln ion, creates lower local distortion [11]. Therefore, we envisage that, depending on type Ln ion, the local structure of the LnCl₆ octahedra changes upon the doping of Sb³⁺ ions. Consequently, the Sb³⁺-doped NCs demonstrate varying luminescence properties depending on the type of Ln of the host NCs. Moreover, the degree of local distortion of a given material is dependent on the average bond length (l_{av}), variance in the distortion angle (σ), and distortion index (D). Therefore, the l_{av} , σ , and D for the various CLnC: Sb³⁺ NCs were calculated. The values of these three parameters increased linearly with the size of the Ln ion. Furthermore, it was also observed that the polyhedra size of the LnCl₆ octahedra increased as a function of the Ln ion size (Fig. 3e). Therefore, these structural calculations suggest that a direct relationship exists between the size of the polyhedra and the local distortion in the CLnC:Sb³⁺ NCs, which influences the tuning of the emission wavelengths and improves the PLQY values in the CLnC:Sb³⁺ NCs. Based on the obtained results, a mechanism for tuning the emission energies in CLnC:Sb³⁺ NCs is proposed in Fig. 3f. When irradiating the CLnC:Sb³⁺ NCs with 320 nm light, electrons in the ground state of ¹S₀ are excited into the ¹P₁ and ³P₁ states. Following this, the electrons from the higher energy excited state, ¹P₁, are transferred to the STE1 stat and radiatively recombine with ¹S₀ causing the 450 nm emission band (Fig. 3a). In contrast, a lower energy excited state transfers the energy to STE2 and radiatively recombines

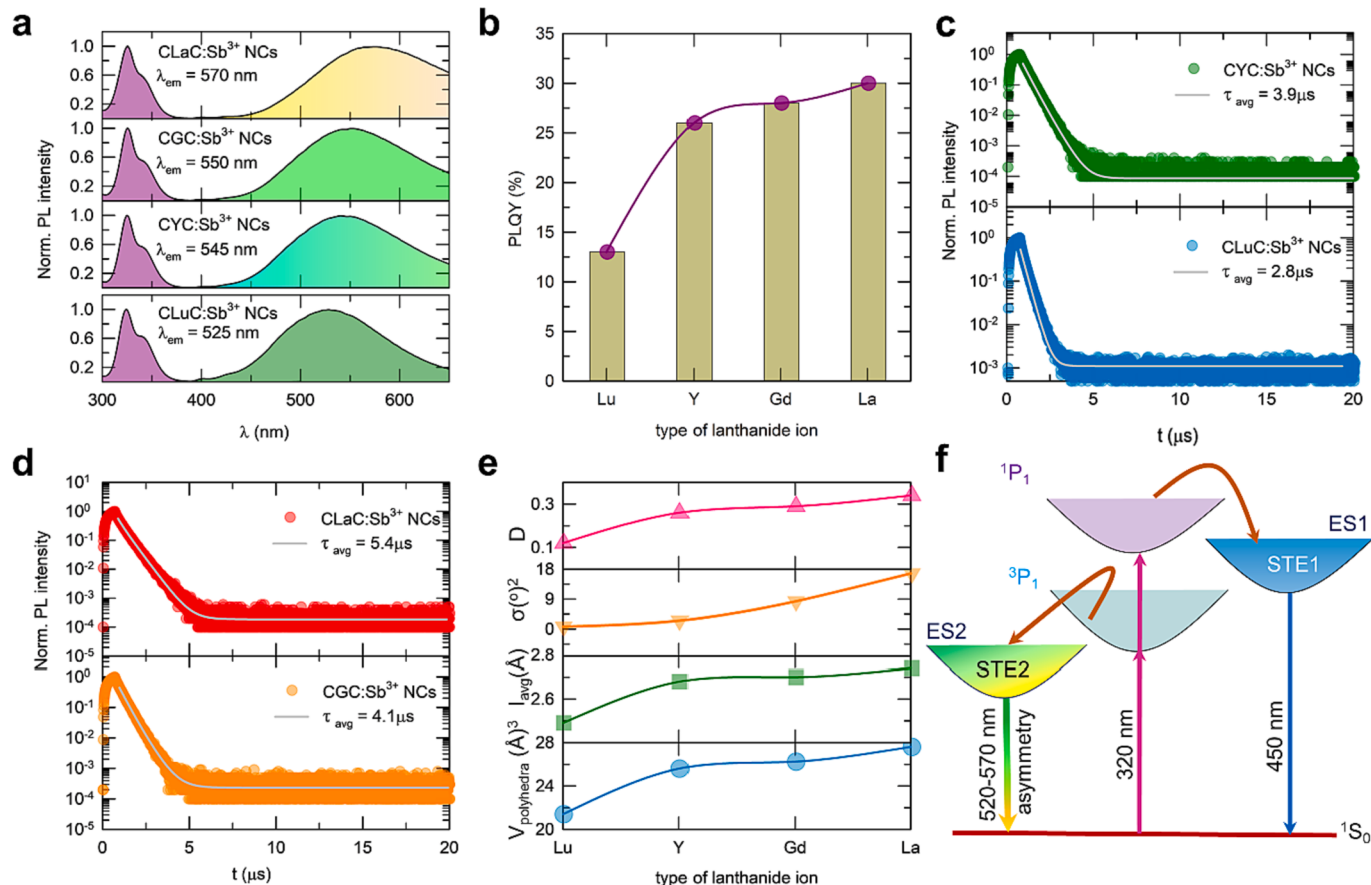


Fig. 3. The luminescence properties of CLnC: Sb³⁺ NCs. (a) excitation and emission spectra of CLnC:Sb³⁺ NCs, under 320 nm excitation. (b) Variation of PLQY values in CLnC: Sb³⁺ NCs, as a function of type of lanthanide ion in Ln-site. (c) and (d) Shows lifetime of CLnC: Sb³⁺ NCs monitored the emission wavelengths of 525 (for CLuC:Sb³⁺ NCs), 545 (for CYC:Sb³⁺ NCs), 550 (for CGC:Sb³⁺ NCs), and 570 nm (for CLaC:Sb³⁺ NCs), respectively. (e) Calculated $V_{\text{polyhedra}}$, l_{av} , σ , and D as a function of type of lanthanide ion in CLnC:Sb³⁺ NCs. These parameters are extracted after full pattern refinement of CLnC: Sb³⁺ NCs. (f) schematic for proposed mechanism for the origin of tuning the emission wavelengths in CLnC: Sb³⁺ NCs, where violet arrow represents the excitation, blue, green-yellow arrows represent the emission wavelengths, and red arrows show the energy transfer from the $1P_1$ and $3P_1$ states to STE1 and STE2, respectively. (For interpretation of the references to color in this figure legend, the reader is referred to the web version of this article.)

with 1S_0 , causing emissions in the green and yellow regions, respectively, depending on the degree of asymmetry present in the LnCl_6 octahedra (Fig. 3f). When Sb³⁺ ions are doped into the host material, two distinct types of STE states are typically excited. The first type corresponds to a higher energy STE state, resulting from the electronic transition from 1P_1 to 1P_0 , which is a spin-allowed transition. The second type involves the formation of lower-lying STE states, which arise from the electronic transition from 3P_n , where n can take values of 0, 1, and 2, to 1P_0 . This transition is classified as a parity-spin-allowed transition. Furthermore, the spin-allowed transition from 1P_0 to 1P_1 is comparatively feeble when compared with the parity-allowed transition from 3P_1 to 1P_0 in zero-dimensional metal halides. This disparity in transition strengths contributes to the observation of broad emission band within the blue-green-yellow spectral regions [28]. In addition, we also observed that there is a feeble blue emission band originating from the CLnC:Sb³⁺ NCs. To understand the emission behavior, we measured the PL spectra of CLaC:Sb³⁺ NCs by illuminating the 320 nm light, exhibits a broad blue emission band (Fig. S4a) and also measured the PL lifetime by monitoring the 450 nm which is lies in the nanosecond's regime (Fig. S4b). As it is noted that, the high-energy emission occurring from the $^1P_1 \rightarrow ^1S_0$ transition is a spin-allowed transition, whose lifetime typically lies in the nanosecond range. Whereas, the low-energy emission originating from the $^3P_n \rightarrow ^1S_0$ transition is a spin-forbidden transition, whose lifetime typically lies in the microsecond range. The underlying cause of this contrast is attributed to the dynamic lone-pair

effect exhibited by Sb³⁺ions to obtain a broad emission band [29–31].

To gain a deeper insight into the optical properties observed in the previous section, the entire lattice of the CLnC:Sb³⁺ NCs was included in the computational model by applying a $2 \times 2 \times 2$ replication of their unit cells. By substituting one Ln atom with one Sb atom, a doping concentration of 2 % was obtained, which is consistent with the experimental results. Fig. 4a-d show that the $[\text{SbCl}_6]_{\text{a}1g}$ state, whose molecular orbitals consist of the 5 s orbitals of Sb, contributes to the valence band maxima (VBM) MOs, whereas the 5p orbitals contribute to the t_{1g} state MOs located within the conduction band. Notably, Lu 5d, Y 4d, Gd 5d, and La 5d orbitals dominated the conduction band minima (CBM) in the CLnC:Sb³⁺ NCs. Despite this, the Lu, Y, Gd, and La transitions are dark in nature. The only optically involved transition was related to the Sb³⁺ ions, which is challenging for DFT because its variational nature always collapses at the lowest energy state for a given spin multiplicity [16]. Therefore, to overcome this problem, the authors chose to qualitatively follow the electronic structure of the CLnC:Sb³⁺ NCs, stretching the Sb-Cl bonds axially at the $[\text{SbCl}_6]^{3-}$ octahedra, and applying an elongation of 0–35 % (Figure S5). Fig. 4a-d show that the anti-MO of Sb(5p)-Cl(3p) decreased faster than the orbital involved in Sb (5 s), which ultimately accounts for the local distortion at the Ln site. However, the amount of local distortion depends on the size of the polyhedra. This causes it to exhibit variable Stokes shifts depending on the degree of local distortion of the LnCl_6 polyhedra. Consequently, the local distortion of LnCl_6 was calculated, revealing that it varied from

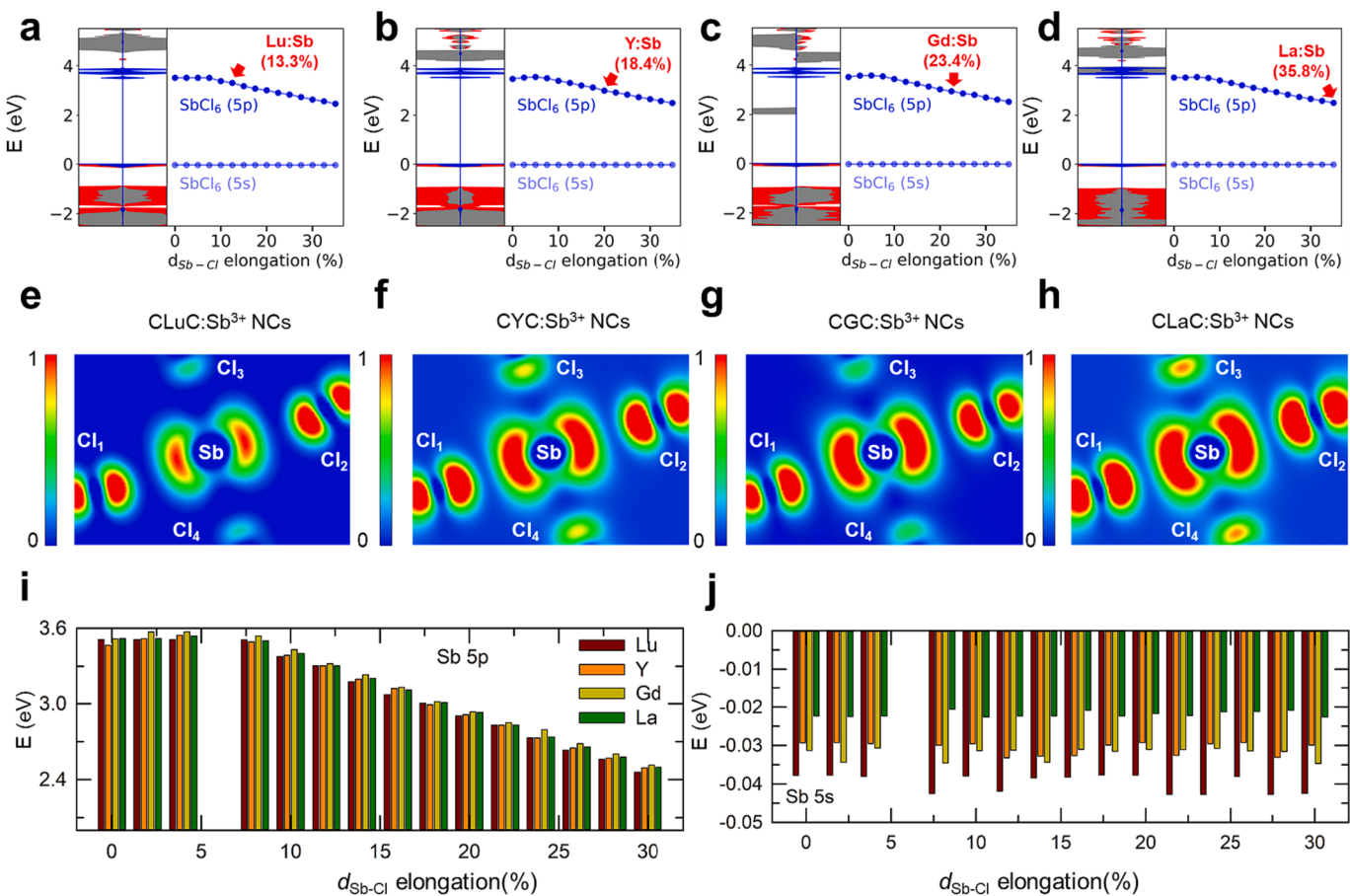


Fig. 4. Computational analysis for the origin of the emission color tuning in the CLnC:Sb³⁺ NCs. Electronic energy levels of (a) the CLuC, (b) CYC, (c) CGC, and (d) CLaC $2 \times 2 \times 2$ supercells doped with one Sb³⁺ ion computed at the DFT/PBE level of theory. The CBM and VBM of the LuCl₆, YCl₆, GdCl₆, and LaCl₆ matrices are depicted with red- and grey-colored lines, whereas, the SbCl₆ matrix is shown with a blue-colored line. (e–h) Partial electron densities around the metal center of Sb with a contour plot of the saturation level between 0.044 e⁻/Å⁻³ (maximum) and 0.002 e⁻/Å⁻³ (minimum) in the CLnC:Sb³⁺ NCs. (i) and (j) show the HOMO and LUMO energies of the lowest electronic transitions involving the SbCl₆ octahedron upon symmetric percentage of elongation of Sb-Cl in the CLnC:Sb³⁺ NCs. (For interpretation of the references to color in this figure legend, the reader is referred to the web version of this article.)

13.3 to 35.3 % with the size of the LnCl₆ polyhedra (Lu to La), which is consistent with the structural outcomes derived from the Rietveld refinement analysis. Additionally, to visualize the local distortion in the CLnC:Sb³⁺ NCs, electron density calculations were performed. Fig. 4e–h show that the electron density around the metal center increased, indicating that the local distortions around this metal center increase with the increasing size of the LnCl₆ polyhedra [32]. Furthermore, the energy gap between the HOMO and LUMO levels in CLnC:Sb³⁺ NCs were extracted, which showed that increasing the elongation of Sb-Cl bond lengths varied the HOMO and LUMO positions (Fig. 4i, j), and the calculated Stokes shift at the equilibrium axial bond for the CLuC:Sb³⁺, CYC:Sb³⁺, CGC:Sb³⁺, and CLaC:Sb³⁺ NCs were 1.45, 1.54, 1.61, and 1.68 eV, respectively, which correlated with the experimental Stokes shift values of the CLnC:Sb³⁺ NCs. Therefore, these results suggest that the degree of local distortion in LnCl₆ was ultimately responsible for the color tuning in the CLnC:Sb³⁺ NCs.

To understand the temperature-dependent PL behavior of the CLaC:Sb³⁺ NCs, their PL properties were measured at 85–250 K. The PLQY of the NCs reached 100 % at low temperatures because of the disappearance of non-radiative emission pathways at very low temperatures. However, an increase in the temperature from 85 to 250 K monotonically reduced the radiative PL intensity of the CLaC:Sb³⁺ NCs (Fig. 5a), which is known as thermal quenching (TQ) [33]. This phenomenon is typically observed in all inorganic LHPs and MHSs, and the thermal stability of any luminescent material depends entirely on the environment of the luminescent center. For example, a material with a

rigid environment around the luminescent center exhibits a weak electron-phonon interaction, leading to minimal TQ at elevated temperatures [34–36]. In particular, soft lattice emitters, such as STE emitters, have a strong electron-lattice interaction, which reduces the radiative PL intensity at elevated temperatures. A similar mechanism also accounts for the TQ in the CLaC:Sb³⁺ NCs because of the soft lattice interactions around the [SbCl₆]³⁻ octahedra. The exciton binding energy was calculated using the Arrhenius equation:[37]

$$I_{\text{CLaC:Sb}^{3+}}(T) = \frac{I_0}{1 + A \exp\left(\frac{-E_b}{K_B T}\right)} \quad (1)$$

where I_0 is the initial PL intensity, $I_{\text{CLaC:Sb}^{3+}}(T)$ corresponds to the PL intensities at different temperatures, E_b is the exciton binding energy, A is a constant related to the non-radiative to radiative rate, and K_B is Boltzmann's constant. Owing to their OD nature, the exciton binding energy of the CLaC:Sb³⁺ NCs was 184 meV (Fig. 5b), which was higher than that of the three-dimensional MHPs (18 meV) [38]. In addition, we also measured the low temperature PL of CLuC:Sb³⁺ NCs, CYC:Sb³⁺ NCs, CGC:Sb³⁺ NCs (Figure S6a-c), and calculated the E_b using the equation-1, exhibits a relatively high E_b values when compared to CLaC:Sb³⁺ NCs (Figure S6d). Typically, NCs with lower E_b often exhibit higher PLQY. This is because lower binding energy facilitates the efficient separation of the electron and hole, reducing the probability of non-radiative recombination processes that can lead to energy loss without photon

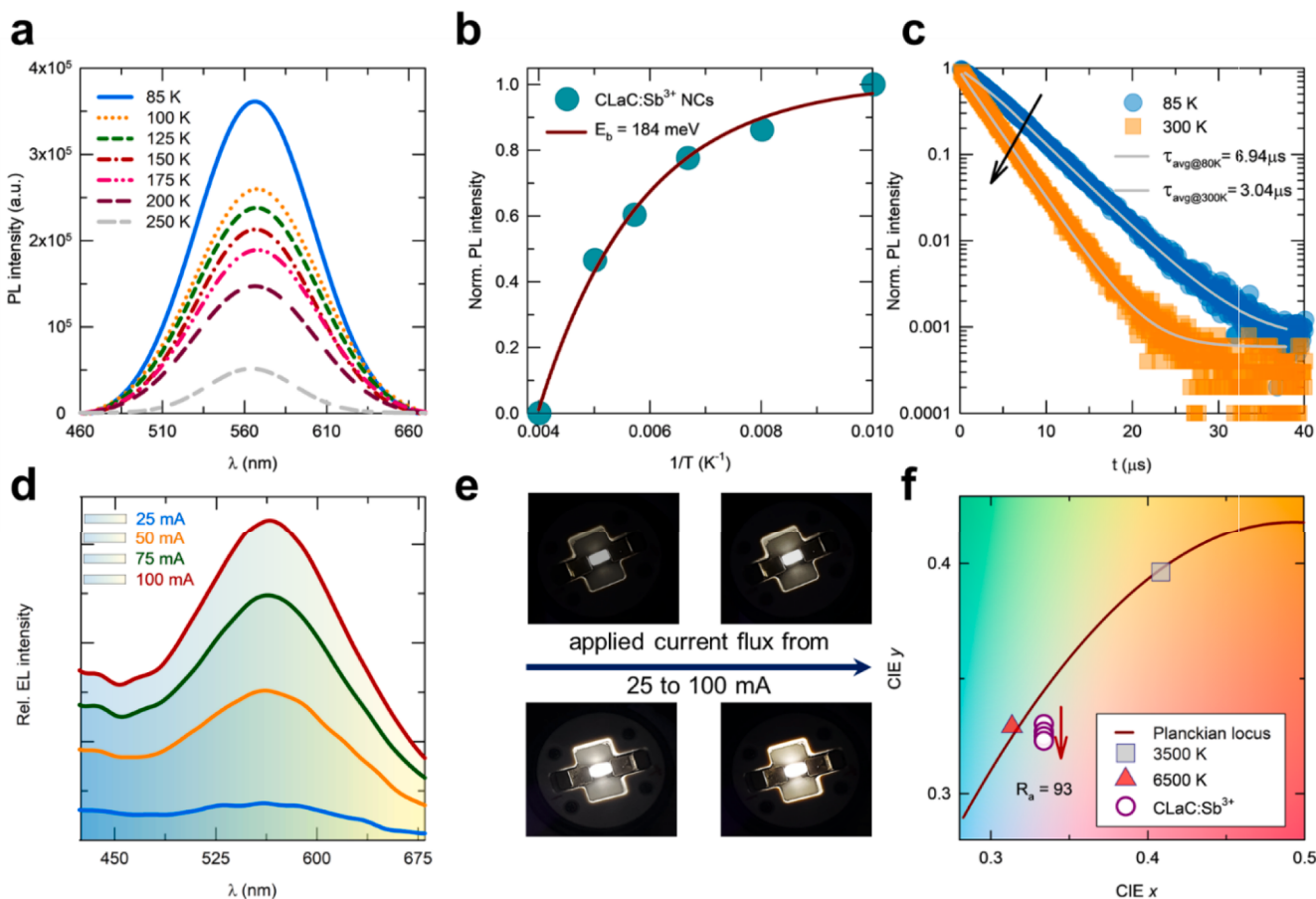


Fig. 5. Temperature dependent luminescence properties of CLaC:Sb³⁺ NCs and performance of fabricated prototype single component WLED using CLaC:Sb³⁺ NCs. Electronic energy levels of (a) low temperature PL properties of CLaC:Sb³⁺ NCs upon heating from 85 K to 250 K. (b) Arrhenius plot for determining the exciton binding energy of CLaC:Sb³⁺ NCs. (c) Temperature dependent time resolve PL lifetime properties of CLaC:Sb³⁺ NCs. (d) EL properties of single component WLED device fabricated using CLaC:Sb³⁺NCs, as a function of applied current flux ranging from 25 mA to 100 mA. (e) Photographic images of fabricated prototype WLED of CLaC:Sb³⁺ NCs at different applied current flux. (f) Color coordinates of CLaC:Sb³⁺ NCs prototype WLED.

emission. The PL lifetime of the CLaC:Sb³⁺ NCs were measured at 85 and 300 K, which demonstrated that increasing the temperature from 85 to 300 K reduced the radiative PL lifetime from 6.94 to 3.04 μs (Fig. 5c). Moreover, a similar trend was observed for the CLaC:Sb³⁺ NCs (Figure S7a), CYC:Sb³⁺ NCs (Figure S7b), and CGC:Sb³⁺ NCs (Figure S7c). Moreover, a comprehensive assessment of the moisture stability of CLaC:Sb³⁺ NCs was conducted over a period of 4 weeks. The results, illustrated in Figure S8, reveal that these nanocrystals exhibited notable resilience by retaining a significant portion of their PL intensity throughout the duration of the test. Furthermore, we subjected CLaC:Sb³⁺ NCs to a photostability test under continuous illumination with 365 nm light. Remarkably, the nanocrystals demonstrated exceptional stability, retaining 97 % of their original PL intensity, as depicted in Figure S9. This outcome underscores the robustness of the material even when exposed to prolonged illumination by UV light for a duration of 8 h. These findings collectively highlight the enduring and reliable performance of CLaC:Sb³⁺ NCs, both in the presence of moisture and under extended exposure to UV light. Single-component WLEDs were fabricated as a proof of concept using C dot-assisted CLaC:Sb³⁺ NCs, and their corresponding their optical properties are shown in Figure S10. The electro luminescence (EL) spectra of the CLaC:Sb³⁺ NCs covered the entire visible region with a corresponding high color rendering index of 93 at 25 mA. Furthermore, the relative EL intensity, and thus brightness, of the WLED increased with an increasing current flux from 25 mA to 100 mA (Fig. 5d, e). Under the high current flux, the color coordinates of the CLaC:Sb³⁺-based WLED are slightly shifted (Fig. 5f), which was attributed to the soft lattice nature of the CLaC:Sb³⁺ NCs. To further

examine the operational stability of the fabricated WLED device, we continuously operated the device for 400 hrs and calculated the luminance efficacy at equal intervals. The original luminance efficacy remains unchanged during the continuous operation for 400 hrs, as shown in Figure S11. Overall, these results suggest that CLaC:Sb³⁺ NCs can be used for solid-state lighting applications.

4. Conclusion

A family of 0D MH CLnC:Sb³⁺ NCs were synthesized using a hot-injection method. Upon illumination with a 320 nm light, the CLnC:Sb³⁺ NCs exhibited distinct emission colors from green to yellow. Furthermore, the PLQY of the NCs increased linearly with the size of LnCl₆. The structural and computational results revealed an interconnection between the local distortion and the size of the polyhedra, which enabled tunable emission color and an improved PLQY. Furthermore, a single-component WLED fabricated using CLaC:Sb³⁺ NCs delivered a high color rendering index value of 93 at 25 mA. Therefore, these results can be used as a platform to tune the emission colors of 0D MHs in the blue, green, and red spectral regions. This strategy can be used to develop full-color-emitting luminescent materials for next-generation solid-state lighting applications.

CRediT authorship contribution statement

Tuhin Samanta: Writing – original draft, Data curation, Conceptualization. **Noolu Srinivasa Manikanta Viswanath:** Conceptualization,

Data curation, Writing – original draft, Writing – review & editing, Visualization, Investigation, Validation, Formal analysis, Methodology, Software. **Heyon Woo Kim:** Data curation. **Sung Woo Jang:** Data curation. **Joo Hyeong Han:** Data curation. **Sung Beom Cho:** Data curation. **Won Bin Im:** Conceptualization, Writing – review & editing, Supervision, Funding acquisition, Resources, Project administration.

Declaration of competing interest

The authors declare that they have no known competing financial interests or personal relationships that could have appeared to influence the work reported in this paper.

Data availability

Data will be made available on request.

Acknowledgement

This work was supported by the National Research Foundation of Korea (NRF) grant funded by the Korea government (MSIT) (NRF-2022M3H4A1A03076093, NRF-2022H1D3A3A01077343, NRF-2021M3H4A1A02049634, and NRF-2020M3H4A3081792).

Appendix A. Supplementary data

Supplementary data to this article can be found online at <https://doi.org/10.1016/j.cej.2024.149697>.

References

- [1] S. Li, J. Luo, J. Liu, J. Tang, Self-trapped excitons in all-inorganic halide perovskites: fundamentals, status, and potential applications, *J. Phys. Chem. Lett.* 10 (8) (2019) 1999–2007.
- [2] J. Luo, X. Wang, S. Li, J. Liu, Y. Guo, G. Niu, L. Yao, Y. Fu, L. Gao, Q. Dong, Efficient and stable emission of warm-white light from lead-free halide double perovskites, *Nature* 563 (7732) (2018) 541–545.
- [3] G.K. Grandhi, N. Viswanath, H.B. Cho, J.H. Han, S.M. Kim, S. Choi, W.B. Im, Mechanochemistry as a green route: Synthesis, thermal stability, and postsynthetic reversible phase transformation of highly-luminescent cesium copper halides, *J. Phys. Chem. Lett.* 11 (18) (2020) 7723–7729.
- [4] K.M. McCall, V. Morad, B.M. Benin, M.V. Kovalenko, Efficient lone-pair-driven luminescence: structure–property relationships in emissive 5s² metal halides, *ACS Mater. Lett.* 2 (9) (2020) 1218–1232.
- [5] J.H. Han, T. Samanta, Y.M. Park, H.J. Kim, N.S. Manikanta Viswanath, H.W. Kim, B.K. Cha, S.B. Cho, W.B. Im, Highly stable zero-dimensional lead-free metal halides for X-ray imaging, *ACS Energy Lett.* 8 (2022) 545–552.
- [6] S. Jin, H. Yuan, T. Pang, M. Zhang, J. Li, Y. Zheng, T. Wu, R. Zhang, Z. Wang, D. Chen, Highly bright and stable lead-free double perovskite white light-emitting diodes, *Adv. Mater.* 2308487 (2023).
- [7] S. Jin, H. Yuan, T. Pang, M. Zhang, Y. He, B. Zhuang, T. Wu, Y. Zheng, D. Chen, Boosting STE and Nd³⁺ NIR luminescence in Cs₂AgInCl₆ double perovskite via Na⁺/Bi³⁺-induced local structure engineering, *Adv. Funct. Mater.* 2304577 (2023).
- [8] S. Jin, R. Li, J. Zhu, T. Pang, T. Wu, H. Zhan, Y. Zheng, F. Huang, X. Chen, D. Chen, Seven-photon absorption from Na⁺/Bi³⁺-alloyed Cs₂AgInCl₆ perovskites, *Mater. Horiz.* 10 (4) (2023) 1406–1415.
- [9] S. Jin, R. Li, H. Huang, N. Jiang, J. Lin, S. Wang, Y. Zheng, X. Chen, D. Chen, Compact ultrabroadband light-emitting diodes based on lanthanide-doped lead-free double perovskites, *Light Sci. Appl.* 11 (1) (2022) 52.
- [10] G.K. Grandhi, H.J. Kim, N. Viswanath, H.B. Cho, J.H. Han, S.M. Kim, W.B. Im, Strategies for improving luminescence efficiencies of blue-emitting metal halide perovskites, *J. Korean Ceram. Soc.* 58 (1) (2021) 28–41.
- [11] L. Mao, Y. Wu, C.C. Stoumpos, B. Traore, C. Katan, J. Even, M.R. Wasielewski, M.G. Kanatzidis, Tunable white-light emission in single-cation-templated three-layered 2D perovskites (CH₃CH₂NH₃)₄Pb₃Br_{10-x}Cl_x, *J. Am. Chem. Soc.* 139 (34) (2017) 11956–11963.
- [12] E.R. Dohner, A. Jaffe, L.R. Bradshaw, H.I. Karunadasa, Intrinsic white-light emission from layered hybrid perovskites, *J. Am. Chem. Soc.* 136 (38) (2014) 13154–13157.
- [13] E.R. Dohner, E.T. Hoke, H.I. Karunadasa, Self-assembly of broadband white-light emitters, *J. Am. Chem. Soc.* 136 (5) (2014) 1718–1721.
- [14] M.D. Smith, B.L. Watson, R.H. Dauskardt, H.I. Karunadasa, Broadband emission with a massive Stokes shift from sulfonium Pb-Br hybrids, *Chem. Mater.* 29 (17) (2017) 7083–7087.
- [15] T. Hu, M.D. Smith, E.R. Dohner, M.-J. Sher, X. Wu, M.T. Trinh, A. Fisher, J. Corbett, X.-Y. Zhu, H.I. Karunadasa, Mechanism for broadband white-light emission from two-dimensional (110) hybrid perovskites, *J. Phys. Chem. Lett.* 7 (12) (2016) 2258–2263.
- [16] D. Zhu, M.L. Zaffalon, J. Zito, F. Cova, F. Meinardi, L. De Trizio, I. Infante, S. Brovelli, L. Manna, Sb-doped metal halide nanocrystals: A 0D versus 3D comparison, *ACS Energy Lett.* 6 (2021) 2283–2292.
- [17] T. Samanta, N.S.M. Viswanath, S.W. Jang, J.W. Min, H.B. Cho, J.H. Han, W.B. Im, Thermally Stable Self-Trapped Assisted Single-Component White Light from Lead-Free Zero-Dimensional Metal Halide Nanocrystals, *Adv. Opt. Mat.* 2202744.
- [18] S.D. Adhikari, C. Echeverría-Arredondo, R.S. Sánchez, V.S. Chirivón, J.P. Martínez-Pastor, S. Agouram, V. Muñoz-Sanjosé, I. Mora-Seró, White light emission from lead-free mixed-cation doped Cs SnCl₆ nanocrystals, *Nanoscale* 14 (4) (2022) 1468–1479.
- [19] J. Jin, Y. Peng, Y. Xu, K. Han, A. Zhang, X.-B. Yang, Z. Xia, Bright green emission from self-trapped excitons triggered by Sb³⁺ doping in Rb₄CdCl₆, *Chem. Mater.* 34 (12) (2022) 5717–5725.
- [20] B. Su, M. Li, E. Song, Z. Xia, Sb³⁺-doping in cesium zinc halides single crystals enabling high-efficiency near-infrared emission, *Adv. Funct. Mater.* 31 (40) (2021) 2105316.
- [21] E. Oomen, W. Smit, G. Blasse, On the luminescence of Sb³⁺ in Cs₂NaMCl₆ (with M= Sc, Y, La): a model system for the study of trivalent s2 ions, *J. Solid State Phys.* 19 (17) (1986) 3263.
- [22] E. Oomen, G. Dirksen, W. Smit, G.J.J.o.P.C.S.S.P. Blasse, On the luminescence of the Sb³⁺ ion in Cs₂NaMBr₆ (M= Sc, Y, La), *J. Solid State Phys.* 20 (8) (1987) 1161.
- [23] K. Momma, F. Izumi, VESTA 3 for three-dimensional visualization of crystal, volumetric and morphology data, *J. Appl. Crystallogr.* 44 (6) (2011) 1272–1276.
- [24] B.H. Toby, EXPGUI, a graphical user interface for GSAS, *J. Appl. Crystallogr.* 34 (2) (2001) 210–213.
- [25] A. Noculak, V. Morad, K.M. McCall, S. Yakunin, Y. Shynkarenko, M. Wörle, M. Kovalenko, Bright blue and green luminescence of Sb (III) in double perovskite Cs₂MnCl₆ (M= Na, K) matrices, *Chem. Mater.* 32 (12) (2020) 5118–5124.
- [26] Y. Zhou, W. Zhuang, Y. Hu, R. Liu, H. Xu, Y. Liu, Y.J.I.C. Li, Second-Sphere Polyhedron-Distortion-Induced Broadened and Red-Shifted Emission in Lu₃(Mg_xAl_{2-x})(Al_{3-x}Si_x)O₁₂:Ce³⁺ for Warm WLED, 58(14) (2019) 9108–9117.
- [27] H. Dong, L.-D. Sun, C.-H. Yan, Local structure engineering in lanthanide-doped nanocrystals for tunable upconversion emissions, *J. Am. Chem. Soc.* 143 (49) (2021) 20546–20561.
- [28] N.S.M. Viswanath, T. Samanta, Y. Yoon, S.W. Jang, K. Kim, W.B. Im, Lone-Pair-Driven, Brightly Emitting Lead-Free Zero-Dimensional Inorganic Luminescent Member, *Adv. Opt. Mat.* 2302565.
- [29] R. Walton, R. Matthews, C. Jorgensen, Absorption spectra of post-transition group halide complexes, *Inorganica Chim. Acta* 1 (1967) 355–359.
- [30] A. Vogler, A. Paukner, H. Kunkely, Photochemistry of coordination compounds of the main group metals, *Coord. Chem. Rev.* 97 (1990) 285–297.
- [31] H. Nikol, A. Vogler, Photoluminescence of antimony (III) and bismuth (III) chloride complexes in solution, *J. Am. Chem. Soc.* 113 (23) (1991) 8988–8990.
- [32] V. Morad, Y. Shynkarenko, S. Yakunin, A. Brumberg, R.D. Schaller, M. Kovalenko, Disphenoidal zero-dimensional lead, tin, and germanium halides: Highly emissive singlet and triplet self-trapped excitons and X-ray scintillation, *J. Am. Chem. Soc.* 141 (25) (2019) 9764–9768.
- [33] Y.H. Kim, N. Viswanath, W.B. Im, Design Principles to Discover Highly Thermally Stable Phosphor, CRC Press, Phosphor Handbook, 2022, pp. 243–264.
- [34] N. Viswanath, M.-H. Fang, H.T. Huu, J.H. Han, R.-S. Liu, W.B. Im, Correlated Na⁺ Ion Migration Invokes Zero Thermal Quenching in a Sodium Superionic Conductor-type Phosphor, *Chem. Mater.* (2021).
- [35] N. Viswanath, G.K. Grandhi, H.T. Huu, H. Choi, H.J. Kim, S.M. Kim, H.Y. Kim, C.-J. Park, W.B. Im, Zero-thermal-quenching and improved chemical stability of a UC₄C₄-type phosphor via crystal site engineering, *Chem. Eng. J.* 420 (2021) 127664.
- [36] Y.H. Kim, P. Arunkumar, B.Y. Kim, S. Unithrattil, E. Kim, S.-H. Moon, J.Y. Hyun, K. H. Kim, D. Lee, J.-S. Lee, A zero-thermal-quenching phosphor, *Nat. Mater.* 16 (5) (2017) 543–550.
- [37] J.H. Han, N. Viswanath, Y.M. Park, H.B. Cho, S.W. Jang, J.W. Min, W.B. Im, Zero-thermal-quenching layered metal halide perovskite, *Chem. Mater.* 34 (12) (2022) 5690–5697.
- [38] L. Protesescu, S. Yakunin, M.I. Bodnarchuk, F. Krieg, R. Caputo, C.H. Hendon, R. X. Yang, A. Walsh, M. Kovalenko, Nanocrystals of cesium lead halide perovskites (CsPbX₃, X= Cl, Br, and I): novel optoelectronic materials showing bright emission with wide color gamut, *Nano Lett.* 15 (6) (2015) 3692–3696.